

Final Draft
of the original manuscript:

Hanke, S.; dos Santos, J.F.:

**Comparative study of severe plastic deformation at elevated
temperatures of two aluminium alloys during friction surfacing**

In: Journal of Materials Processing Technology (2017) Elsevier

DOI: [10.1016/j.jmatprotec.2017.04.021](https://doi.org/10.1016/j.jmatprotec.2017.04.021)

Comparative Study of Severe Plastic Deformation at Elevated Temperatures of two Aluminium Alloys during Friction Surfacing

S. Hanke*, J.F. dos Santos

Helmholtz-Zentrum Geesthacht, Institute of Materials Research, Materials Mechanics, Solid State Joining Processes, Max-Planck-Straße 1, Geesthacht, Germany

*stefanie.hanke@uni-due.de

Abstract

Aluminium alloys 5083 and 6082 were deposited by Friction Surfacing (FS) under the same process conditions. Process characteristics including torque and forces, temperatures and the deposit microstructure were compared. The observed differences are discussed with regard to material strength, thermal softening rate and recrystallization mechanisms.

AA 6082 plasticises faster, reaching $\approx 30\text{K}$ higher temperatures, thicker and wider coatings and a higher material efficiency. The specific energy required for plastification is in the same order of magnitude as the activation energy for self-diffusion, emphasising the influence of dynamic recrystallization (DRX) mechanisms. A tendency for lower grain size and larger variations in grain boundary misorientation observed for AA 5083 points towards a shift in the steady-state DRX balance towards dislocation generation, due to the higher Mg content of this alloy. This corresponds to the lower process speeds required for AA 5083. AA 6082 may undergo more localized shear because of its high thermal softening rate and additional loss of strength through dissolution of Mg_2Si with increasing temperature. This may contribute to a higher energy and material efficiency for plastification and deposition of AA 6082 by FS.

Keywords: thermomechanical processing, dynamic recrystallization, friction surfacing, aluminium alloys, EN AW 6082, EN AW 5083

1 Introduction

Friction Surfacing (FS) is used to apply metal based coatings in solid state, i.e. without bulk melting of the material being deposited. For this reason, it is of particular interest for

materials which are considered to be difficult or impossible to deposit by fusion methods. For example, FS of NiAl bronze was reported by Hanke et al. (2011), of Cr60Ni40 by Hanke et al. (2013) and for steel on aluminium substrate by Chandrasekaran et al. (1997). The applicability of FS to aluminium alloys and the influence of process parameters on dimensions of deposited layers have been demonstrated for AA 5052 by Sakihama et al. (2003) and for AA 6082 by Gandra et al. (2013). The microstructure refinement during FS of AA 6082 has been investigated by Suhuddin et al. (2012), who concluded that significant grain refinement through both continuous and discontinuous recrystallization occurred.

Photographs of different stages during an FS process run are presented in Figure 1. The surfacing process begins with a pre-heating phase during which a rotating stud made from the coating material is pressed with a defined axial force onto the substrate to be coated. The initial relative sliding between the contacting surfaces causes frictional heating of both stud and substrate material. When suitable parameters are chosen the temperature rises fast, within few seconds, and due to the heat flow conditions its maximum is located within the stud tip. This hot material begins to adhere to the substrate surface and the frictional torque causes the thermally softened stud material to flow. Now the difference in motion between the rotating stud and the stationary substrate is no longer borne in the interface between them, but within a shear zone in the softened stud material (Figure 1 (b)). The soft, plastically deforming stud material is often referred to in the literature as “quasi-liquid layer”, e.g. in a study on the potential of FS for repair welding by Tyayar (1959), or “real rotational contact plane” by Fukakusa (1996) in a study on the material flow during FS of steel and by Liu et al. (2008), who investigated the feasibility of applying contact melting theory for studying the FS process. When this plasticised material state is reached, a transversal movement is superimposed. Along the trajectory part of the softened material from the stud tip is deposited onto the substrate, leaving a coating of a width similar to the stud diameter (Figure 1 (c)). Along the outer edge of the stud the softened material cannot fully transfer the axial forging force onto the substrate, resulting in a local lack of bonding present in a narrow region along the edges of each coating layer. Additionally, part of the soft material from the stud’s periphery is squeezed out of the contact zone by the axial force and is pushed upwards around the stud forming a flash, as shown by Fukakusa (1996). The length of a single deposit is limited

by the length of the consumable stud, which may additionally be effectively reduced by the size of the flash moving up towards the stud fixture.

Thickness and width of the coating layer as well as the bonding quality are affected by the process parameters, especially axial force, rotational and translational speed. The effects of process parameters on the deposit characteristics have already been discussed by Tyayar (1959), who showed that the efficiency of the process, i.e. the fraction of the stud actually deposited, changes with the rotational speed of the stud. Still, the rotational speed, axial pressure and translational speed interact with each other and process stability is only given within a certain parameter window. It is generally described that within the range of parameters suitable to produce bonded coatings in a stable process the material efficiency (deposited material yield) as well as the coatings' thickness and width decrease with increasing axial pressure and rotational speed. This tendency was reported by Fukakusa (1996) for stainless steel, by Shinoda et al. (1998) for AISI440C (X105CrMo17; 1.4125) stainless steel on low carbon structural steel (SM490A), and for aluminium coatings (stud and substrate from 5052 alloy) by Sakihama et al. (2003). One exception is Ti-6Al-4V, for which in a study investigating a very wide range of rotational speeds (300 to 6000 min^{-1}), more complex interactions were observed by Fitseva et al. (2016).

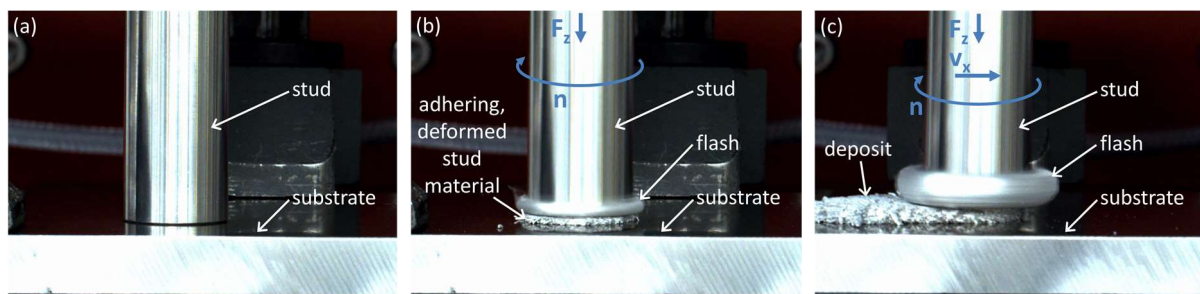


Figure 1: Initial contact between stud and substrate (a), pre-heating and onset of plastification (b) and running FS process (c).

The FS process often results in a fine and homogeneous coating microstructure since the material is deposited in solid state under a high degree of plastic deformation followed by rapid cooling, as shown by Hanke et al. (2011) observing refinement and spheroidization of precipitates in NiAl-bronze and Sakihama et al. (2003) who found grain refinement through

recrystallization in AA 5052. Similar or comparable conditions are found in other friction based joining processes, e.g. Friction Stir Welding.

The parameter window in which FS runs with stable process forces and torque, resulting in coatings of homogeneous width, thickness and defect free bonding varies for different alloys. The application of the process to new materials is generally based on experience as well as trial and error. This is understandable since the deposit material is processed under very specific conditions including a high temperature, for which little is known in terms of material properties and deformation behaviour. Additionally, plastic flow behaviour can depend strongly on the microstructural state and small changes in alloy composition. Donati and El Mehtedi (2011) applied hot torsion tests with up to ten revolutions to AA 6082 sourced from four different suppliers; varying slightly in alloy composition. The peak stress observed varied by approximately 30% and the strain to fracture by up to 500% for the different alloys. At a testing temperature of 500°C these differences significantly lessened, which was related to a diminishing influence of the strengthening precipitates.

In the present work FS was applied to two Al-alloys: solid-solution strengthened AA 5083 and precipitation hardenable AA 6082. The applicable process parameters and the different responses including process temperatures, forces and deposition efficiency as well as the recrystallized microstructure in the deposits are investigated and compared. This study has been devised to understand process and deposit characteristics when applying the same process parameter set to the two different alloys, and to elaborate how the parameters must be adjusted for each alloy in order to obtain comparable deposit geometries. Specific parameter sets were selected in order to fulfil these requirements. The main objective of this work is to identify and quantify the characteristic differences in material behaviour. Furthermore, possible causes for the variety of suitable process parameters and process features observed when changing the alloy composition are discussed.

2 Materials and Methods

2.1 Alloys

Within the scope of this work FS deposits were generated from solid-solution strengthened AA 5083 and precipitation hardenable AA 6082. Their chemical compositions according to DIN EN 573-3:2013-12 (DIN EN 573, 2013) are given in Table 1. The bars were in wrought state, and machined to studs with 20 mm diameter and 120 mm length. AA 6082 was in T6 temper, with a hardness of 98 ± 1 HV0.2, while AA 5083 was in H1 temper and exhibited a hardness of 84 ± 2 HV0.2.

All deposits were applied onto AA 2024 substrate plates measuring 300 x 100 x 10 mm. Degreasing with ethanol was the only surface preparation applied. Some thermal and mechanical properties of the alloys are summarized in Table 2. Due to the lack of published properties under torsional shear, mechanical properties from high temperature tensile tests are given here.

alloy	element [weight%]								
	Si	Fe	Cu	Mn	Mg	Cr	Zn	Ti	Al
AA 6082	0.7-1.3	0.5	0.1	0.4-1.0	0.6-1.2	0.25	0.2	0.1	bal.
AA 5083	0.4	0.4	0.1	0.4-1.0	4.0-4.9	0.05-0.25	0.25	0.15	bal.

Table 1: Chemical composition according to DIN EN 573-3:2013-12 for AA 6082 and AA 5083 (DIN EN 573, 2013).

alloy	solidification range [°C]	thermal conductivity [W/Km]	room temperature	true peak	true peak
			yield strength [MPa]	stress [MPa] at ≈ 0.001 s ⁻¹ and 450°C	stress [MPa] at ≈ 0.001 s ⁻¹ and 350°C
AA 6082	585-650 (*1)	170-220 (*1)	T6: ≥ 255 (*2)	T4: 23 (*3) T7: 14 (*4)	T7: 42 (*4)
AA 5083	585-650 (*1)	110-140 (*1)	H1: ≥ 215 (*2)	30 (*5)	H2: 75 (*6)
AA 2024	521-650 (*1)	130-200 (*1)			

Table 2: Some thermal and mechanical properties of the employed alloys. Data from *1 (Altenpohl, 2005); *2 (DIN EN 485, 2013); *3 (Soliman et al., 2010); *4 (El-Danaf et al., 2008); *5 (Hosseini pour, 2009); *6 (Darras et al., 2015).

2.2 Process Study

2.2.1 Friction Surfacing Process

The equipment used has been custom-designed for the development of friction-based processes and provides the required stiffness for potentially high process forces. It delivers up to 60 kN axial force, a maximum spindle torque of 200 Nm and 6000 min⁻¹ rotational speed. It is equipped with sensors for monitoring of forces in three directions and a torque sensor assembled in the spindle. Additionally, the stud position and machine table x-, y- and z-coordinates are recorded during processing. The axial force is applied and controlled through an electric ball-screw drive and a dynamic electric motor for the spindle provides a constant rotational speed. Further details on the equipment have been described by Fitseva et al. (2015).

The substrate plates were placed on a 10 mm thick AA 2024 backing plate clamped onto the grooved machine platform, in order to ensure repeatable heat flow conditions for all experiments.

The surfacing process itself was accomplished by positioning the stud, rotating at the set rotational speed, onto the start position and applying the set axial force. Preliminary experiments have shown that when the stud shortening in the start position reached 0.8 mm sufficient initial plastification was reached. The translational movement was then automatically triggered. The deposition process was finished, i.e. the rotating stud lifted off the deposited material, when either the generated flash touched the stud fixture (i.e. the stud material was used up), or a deposition length of 130 mm was reached. The deposits were left to cool in air for a few minutes to reach room temperature, and then unclamped.

FS of AA 6082 has been described in the literature by Gandra et al. (2013) and Suhuddin et al. (2012). Therefore, feasible parameters were known from previous work. In the current study, first a parameter range was established, which is applicable to both alloys. In a second step, parameter sets resulting in similar coating geometries were determined. For further comparative analysis of process characteristics and microstructure, five exemplary parameter sets were selected. Each set was applied three times. Parameter sets resulting in a stable FS process do lead to highly reproducible results.

2.2.2 Data Evaluation and Processing

As mentioned above the position of the stud on the z-axis and the position of the machine table in x- and y-direction were recorded over time. While the positions were set to zero for the location where the cold stud tip first touched the substrate surface under the set process force, the absolute process time may vary depending on the machine set-up conditions and any movements or other initial actions carried out after the process was initiated. Data was recorded at a rate of 100 Hz. For further analysis of the process several characteristic values were calculated from the measured data.

The deposition efficiency η is the ratio of the deposited material volume (V_{deposit}) over consumed stud volume (V_{consumed}), i.e. it reveals which fraction of the processed stud material was deposited, and which was lost to the flash. It was calculated according to equation (1)

$$(1) \quad \eta = \frac{V_{\text{deposited}}}{V_{\text{consumed}}} \cdot 100 \% = \frac{d \cdot w \cdot v_x}{\pi \cdot r^2 \cdot v_{\text{CR}}} \cdot 100 \%$$

with the following variables: deposit thickness (d), deposit width (w), translational speed (v_x), stud radius ($r = 10 \text{ mm}$) and stud consumption rate (v_{CR}).

The stud consumption rate v_{CR} is the rate at which the stud is fed into the process in axial (z-) direction while the machine control maintains the set axial force. It therefore relates to the speed at which the stud material is consumed through plastification, deposition and flash formation. It can be calculated from the measured stud position on the z-axis (s_z) over time (t) according to equation (2).

$$(2) \quad v_{\text{CR}} = \frac{\Delta s_z}{\Delta t}$$

FS, as other friction-based joining technologies, introduces only mechanical energy into the material. The introduced power (P) has a torsional component (P_T) as well as axial (P_z) and transversal (P_x) components, as described by equations (3) and (4).

$$(3) \quad P = P_T + P_x + P_z$$

$$(4) \quad P = (2 \cdot \pi \cdot n \cdot T) + (F_x \cdot v_x) + (F_z \cdot v_{\text{CR}})$$

The data used for these calculations additionally include the rotational speed (n), measured torque (T) and forces in x- and z-direction (F_x , F_z).

The contributions of these three components to the total energy used during FS are of different orders of magnitude and influence the processed material in different ways. The torsional component makes up the largest contribution to the energy input (see section 3.2) and enables, together with the power component in stud axial direction, the plastification of the material through severe shear deformation. The component in x-direction is mainly related to the removal of plasticised material from the stud tip and its deposition. Since the energy component from the translational movement is < 1% of the total energy it was neglected in the present considerations. In order to estimate the energy required for heating and plastic deformation of the stud material the specific energy input per consumed stud material volume (e_s) was calculated by equation (5), assuming that the power is introduced across the full stud cross section with a radius of $r = 10$ mm.

$$(5) \quad e_s = \frac{P_T + P_z}{\pi \cdot r^2 \cdot v_{CR}}$$

Previous investigations have shown that it is reasonable to assume that the material transferred into the flash and the deposited material do not undergo the same amount of deformation. Therefore, they do not experience the same energy input. In order to consider the effect different material deposition efficiencies may have on the specific energy input a method suggested by Fukakusa (1996) was used. This approach is based on the observation that only the material from the centre of the stud cross section is deposited as coating layer, while the flash is formed from the outer material. From studies using marker material and filled studs Fukakusa concludes that only the inner material, which is deposited, undergoes the severe torsional shear deformation within what he calls the “real rotational contact plane”. Setting equal the volume of deposited material and a consumed volume from the centre of the stud (equation (6)), the radius of the stud core undergoing torsional deformation can be calculated; here referred to as corrected radius (r_c). In the following calculations Δl is the difference in stud length before and after the process.

$$(6) \quad V_{\text{deposit}} = \pi \cdot r_c^2 \cdot \Delta l$$

$$(6.1) \quad d \cdot w \cdot v_x = \pi \cdot r_c^2 \cdot v_{CR}$$

$$(6.2) \quad r_c = \sqrt{\frac{d \cdot w \cdot v_x}{\pi \cdot v_{CR}}}$$

The word “plane” used by Fukakusa indicates a two-dimensional process zone, which is not a suitable description considering the occurring plastic deformation. Therefore, the term “shear zone” will be used in this work. For a detailed understanding and a precise quantitative analysis of the deformation state in this zone, a comprehensive mathematical model will be required in the future. Still, the torsional deformation acting within the shear zone can be approximated, neglecting the axial load for simplicity (see sections 4.3 and 4.4 for further discussion). The engineering torsional shear strain (γ) is defined here as the distance travelled by a discrete material element on the circumference of the cylindrically shaped shear zone divided by its thickness, as given in equation (7). Here, (N) is the number of rotations, (r) is the radius of the sheared layer and (h) is its thickness. The same approach is used in the analysis of high-pressure torsion experiments, e.g. by Zhilyaev and Langdon (2008). γ as well as the maximum torsional shear stress (τ) during FS were calculated according to the simple equations (7.1) and (8).

$$(7) \quad \gamma = \frac{2 \cdot \pi \cdot N \cdot r}{h}$$

$$(7.1) \quad \gamma = \frac{2 \cdot \pi \cdot n \cdot r_c}{v_{CR}}$$

$$(8) \quad \tau = \frac{2 \cdot T}{\pi \cdot r_c^3}$$

2.2.3 Temperature Measurements

Thermocouples type K were used to measure the temperature in the interface between the stud and the coating, in the instant when it is deposited. This was accomplished by drilling holes of 0.8 mm diameter into the substrate plate, feeding the thermocouples in from the back side and positioning the tip at the same height as the substrate surface. The trajectory of the translational movement was set to pass over the thermocouples with the centre of the stud cross section, at the half length of the deposited layer. Data was recorded at 100 Hz during the deposition process and the following cooling down to 30°C.

An infra-red (IR) camera (ImageIR 8300, Infra Tec GmbH, Dresden, Germany) was utilized to observe the temperatures on the surface of the stud and the deposited material during deposition. It was placed in front of the welding machine, with the direction of view

perpendicular to both translational movement in x-direction and stud feed in z-direction (i.e. observing the process “from the side”). The field of view was fixed on the stud and during the translational movement the active shear zone at the stud tip remained in the camera’s focus. The temperature range set for the measurements was 150 to 750°C, and thermograms of the running process were recorded at 80 Hz. The reflectivity of a material’s surface affects IR measurements significantly and depends on many factors including the surrounding atmosphere, the surface contour, oxide film thickness and the angle of measurement. Therefore, after the conclusion of one deposition run a thermocouple was applied to the hot surface of deposited material and compared to the IR measurement. The emission factor was close to 1, possibly due to the rough and oxidized surface of the coatings.

2.3 Metallographic Investigation

Samples were extracted from the deposited material and the substrate underneath, with the cutting direction perpendicular to the translational deposition direction. The cross sections were prepared by mechanical polishing according to standard metallographic practice. For Electron Backscatter Diffraction (EBSD) a vibratory polisher (VibroMet 2, Buehler, Illinois, USA) was used for the final preparation step, exposing the samples to 0.05 µm grain size Silica suspension for approximately 12 h.

Scanning Electron Microscopy (SEM) (Quanta FEG 650, FEI Europe B.V., Eindhoven, The Netherlands) and EBSD (Digiview IV CCD camera & TSL OIM Analysis 7, EDAX Inc., Mahwah, USA) were employed to investigate the coatings’ microstructure. Measurements were carried out at 15 kV acceleration voltage, a working distance of 17 mm and at two different resolutions. At a magnification of 2000x, areas of 70 x 70 µm were scanned at a step size of 0.2 or 0.1 µm in order to observe microstructural features inside the grains or of the grain boundaries. At a magnification of 500x, scans of 250 x 250 µm were obtained at a step size of 0.5 µm for statistical analysis of grain size and grain boundary misorientation. Only fcc Al was indexed in the EBSD maps. The data was cleaned through removing pixels with a confidence index ≤ 0.5 , thereby eliminating measurement points from precipitates.

3 Results

3.1 Process Parameter Window and Deposition Efficiency

The main process parameters axial force (F_z), rotational speed (n) and translational speed (v_x) were varied initially in a wide range. The range within which both alloys can be deposited in a quality suitable for further investigation, i.e. continuous, homogeneous layers of a thickness of > 0.5 mm, is rather limited, as presented in Table 3. Various combinations of the parameter values given here can be used to obtain material deposition in varying shapes and qualities. The boundaries of this parameter window can be understood from the macroscopic images of deposits shown in Figure 2. For high rotational and translational speeds and low axial force the deposit layers tend to be thinner for both alloys. AA 5083 always produces a lower deposit thickness than AA 6082 when applying the same parameters, thereby limiting the upper values for the process speeds (compare Figure 2 (a) and (b)). When applying a rotational speed higher than 2000 min^{-1} or a translational speed of more than 15 mms^{-1} to AA 5083 instabilities occur in the process, the deposited layer contains gaps, and the stud may bend and even fracture due to sudden increases in process forces (see also section 3.2). AA 6082 can be well processed at higher speeds and lower axial force. At low speeds and high axial force AA 5083 depositions are thick and homogeneous, but AA 6082 depositions grow strongly in vertical direction, also forming a large amount of flash and consuming the stud very fast (compare Figure 2 (c) and (d)).

parameter	varied range					
axial force F_z [kN]	9		12		16	
rotational speed n [min^{-1}]	1000	1500	1700	2000		
translational speed v_x [mms^{-1}]	2.5	5.5	7.5	10	12	15

Table 3: Parameter window applicable both to AA 6082 and AA 5083, as used in this study.

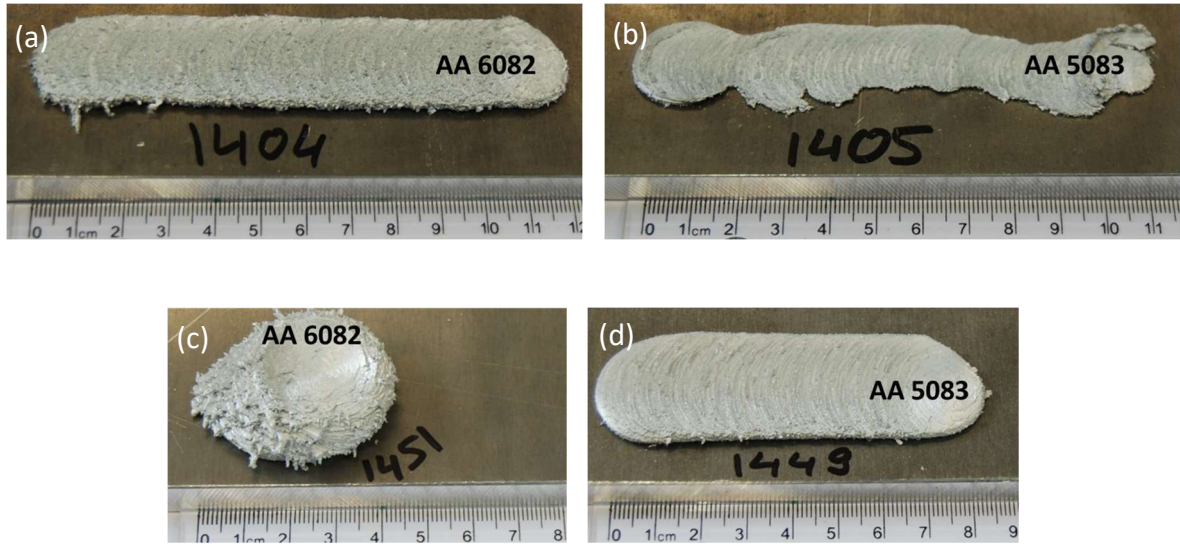


Figure 2: Appearance of deposits from the two Al alloys generated with process parameters at the boundaries of the operable parameter window. $F_z = 9 \text{ kN}$, $n = 2000 \text{ min}^{-1}$ and $v_x = 15 \text{ mm s}^{-1}$ (a) and (b); $F_z = 16 \text{ kN}$, $n = 1000 \text{ min}^{-1}$ and $v_x = 2.5 \text{ mm s}^{-1}$ (c) and (d).

The width and thickness of deposits from both alloys, generated with selected parameter sets, are shown in Figure 3 (a). The influence of process parameters on FS deposit geometry has been examined in detail in various publications (see section 1) and shall therefore not be discussed further here. Figure 3 (b) presents the deposition efficiency for the same parameter sets. The higher deposition volumes obtained for AA 6082 bring about a higher deposition efficiency as well, compared to AA 5083 at the same parameters. The efficiency ranges between 22 and 40% for AA 5083 and 58 to 75% for AA 6082, while the values do not directly correlate with the deposit width or thickness.

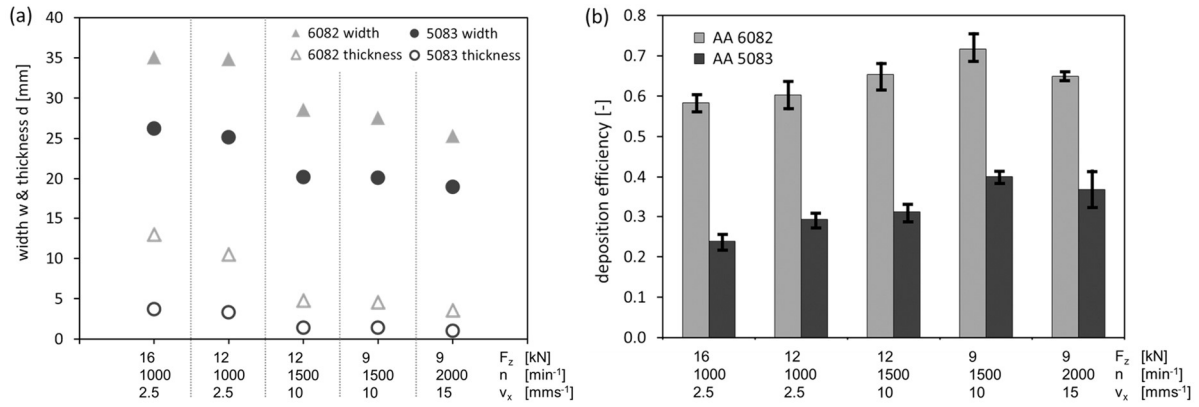


Figure 3: Coating width and thickness (a) and deposition efficiency (b) of AA 5083 and AA 6082 FS deposits for selected parameter sets.

3.2 Process Forces and Torque

The measured values of the axial force (F_z), the force acting in opposite direction to the translational movement (F_x), the position of the stud on the translational path (s_x) as well as the torque measured in the spindle (T) are drawn for process runs with the same parameters for AA 6082 and AA 5083 in Figure 4. For AA 6082 a higher material volume is deposited and the stud is consumed faster, resulting in a shorter deposit length (= end value of s_x) and process time (t) (Figure 4 (a)). For both alloys fluctuations in the axial force occur during initial plastification. In particular for AA 6082 the force during the plastification phase remains below the set value of 9 kN. The translational movement is triggered when the stud has initially shortened by 0.8 mm due to plastification and material flow. As the stud starts to move across the substrate (deposition phase), F_z rises for AA 6082 and stabilizes at the set value. AA 5083 on the other hand shows heavy fluctuations in the range of ± 2 kN, which are compensated after approximately 3 s (Figure 4 (b)). The force in deposition direction (F_x) oscillates around 500 N for AA 6082, while for AA 5083 it rises during the first seconds of deposition to a stable value of 1.1 kN. Large force fluctuations and building up of a transversal force is regularly observed for AA 5083 and can even lead to bending and fracture of the stud. In contrast, AA 6082 tends to small range oscillations which – given a suitably stiff processing equipment as used in this work – do not cause process interruptions. The torque acting during FS is higher in the beginning of initial plastification and attains a stable value during steady-state deposition within the parameter window investigated (compare Figure 4 (a) and (b)).

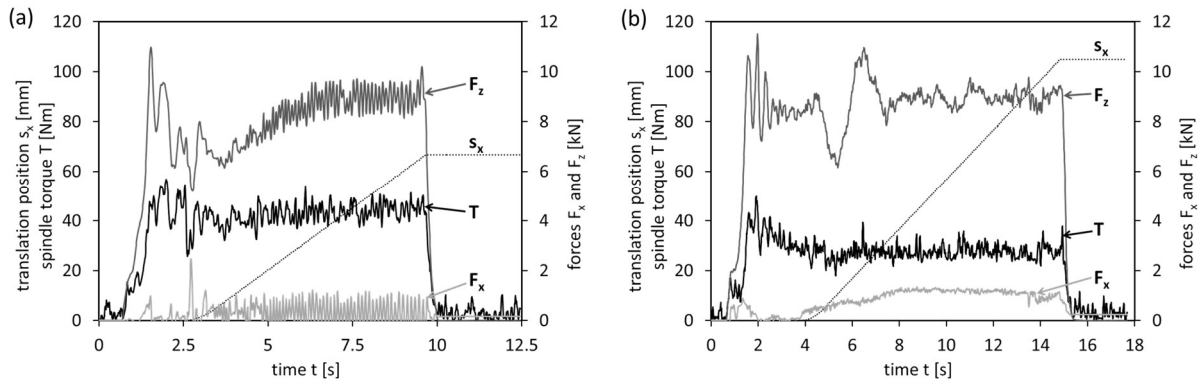


Figure 4: Forces F_z and F_x , spindle torque T and translational distance travelled by stud s_x during FS process runs with $F_z = 9$ kN, $n = 1500$ min⁻¹ and $v_x = 10$ mms⁻¹, over process time t . Shorter process time for AA 6082 is due to faster stud consumption (a); AA 5083 displays fluctuations in F_z and increasing F_x as translational motion sets in (≈ 10 s), while the torque is generally lower (b).

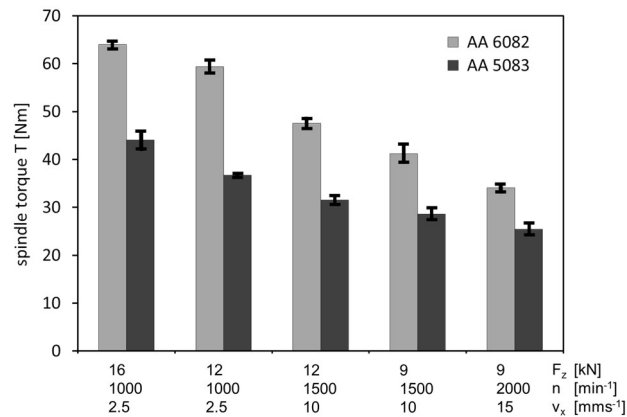


Figure 5: Average torque T during steady-state deposition for selected parameter sets.

Average torque values during steady-state deposition of the two alloys are presented in Figure 5. For AA 6082 the torque is always higher than for AA 5083. It decreases, and the difference between the two alloys diminishes, with the order at which the parameter sets are displayed. This order was chosen according to decreasing axial force and increasing rotational and translational speeds (i.e. decreasing width and thickness of deposited material).

3.3 Stud Consumption and Specific Energy

In Figure 6 (a) the stud consumption rates (v_{CR}) are shown for the two process runs presented in Figure 4. At $t = 0$ s the rotating stud touches the substrate and the plastification begins. The vertical dashed lines indicate when the stud shortening of 0.8 mm is reached and the

deposition stage starts. For AA 6082 this takes 1.6 s, while for AA 5083 2.8 s are required. Faster initial plastification of AA 6082 compared to AA 5083 at the same process parameters was observed in all experiments. For both alloys the consumption rate increases as the translational movement sets in. While AA 6082 shows a continuous rise until a stable value of 7.47 mms^{-1} is reached, AA 5083 shows some fluctuations before it also reaches a constant, but significantly lower value of 2.36 mms^{-1} . The evolution of v_{CR} in the early deposition stage correlates well with the axial force acting at the same time (compare Figure 4).

The average stud consumption rate during steady-state deposition for different parameter sets is presented in Figure 6 (b), one value for AA 5083 being not available. The consumption of AA 6082 occurs significantly faster for all parametric combinations shown, with consumption rates ranging from 5.3 to 9.5 mms^{-1} , when compared with the AA 5083 (2.3 to 3.8 mms^{-1}). The consumption rates show no clear correlation with the deposition efficiency (Figure 3 (b)) and the torque (Figure 5).

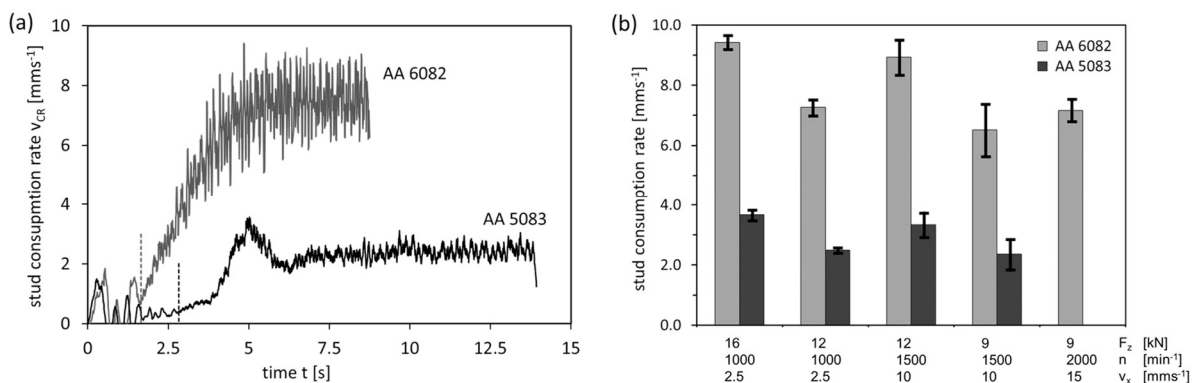


Figure 6: Stud consumption rate v_{CR} during two FS process runs with $F_z = 9 \text{ kN}$, $n = 1500 \text{ min}^{-1}$ and $v_x = 10 \text{ mms}^{-1}$, over process time t (a). At $t = 0 \text{ s}$ the rotating studs first touch the substrate. The dashed vertical lines indicate the onset of v_x . Average v_{CR} during steady-state deposition are shown in (b).

The corrected radius (r_c), corresponding to the fraction of material deposited from the stud core acc. to equation (6.2), is presented in Figure 7 (a). This figure also shows two values for the specific energy input during steady-state deposition, i.e. the amount of energy required for the consumption of 1 mm^3 of stud material. The nominal value (e_s) relates P_T and P_z to the full stud cross section. The values denominated e_{sc} take into account the corrected radius. It was considered in their calculation, that P_T is only introduced into the “real rotational contact

plane”, while P_z is introduced into the complete stud cross section, contributing both to the torsional plastic deformation and the flash formation. The corrected radii correlate with the deposition efficiency (Figure 3 (b)) since a larger fraction of material going into the flash, due to a variation of process parameters, leads to a smaller corrected radius. This is particularly pronounced for the low deposition efficiencies of AA 5083. The nominal specific energy needed to process AA 5083 is higher than that for AA 6082, due to lower stud consumption rates and therefore smaller amounts of processed material. The values of the corrected specific energy for the two alloys lie even further apart since the torsional power input is only introduced into the corrected radius. Although this approach provides an imperfect description of the real situation and the obtained energy values must be considered as approximation, the significant differences in energy consumption of the two alloys during FS are clearly revealed. While e_{sc} for AA 6082 ranges between 5.2 and 6.8 Jmm⁻³, AA 5083 requires 15.9 to 19.8 Jmm⁻³. Considering simply the molecular volume of pure Aluminium of $10 \cdot 10^{-6} \text{ m}^3\text{mol}^{-1}$, the values mentioned approximate to 52 to 68 kJmol⁻¹ for AA 6082 and 159 to 198 kJmol⁻¹ for AA 5083.

In Figure 7 (b) the shear strain and stress acting on the corrected radius r_c , are presented. The shear strain is significantly higher for AA 5083, due to the alloy’s low stud consumption rates, which cause the stud material to remain within the shear zone for a longer time. Therefore, each material volume undergoes a higher number of rotations, before being deposited. E.g. considering a stud consumption rate of 6 mms⁻¹, at a rotational speed of 2000 min⁻¹, these 6 mm of stud length theoretically undergo 33.3 full rotations within 1 s. A 1 mm thick disc of the stud cross section would therefore experience 5.6 rotations. A lower stud consumption rate of e.g. 2 mms⁻¹ would lead to the 1 mm thick disc undergoing 16.7 rotations. Although these considerations are very useful for comparison of the two alloys, a major uncertainty is the fact that the degree of shear localization is not known. It is not clear how the torsional deformation is distributed over the stud in axial direction. The maximum torsional shear stress encountered on r_c , neglecting the influence of the axial force on material flow, is always higher for AA 5083. This correlates with the mechanical properties at elevated temperatures presented in Table 2. The values are reasonable, e.g. at $F_z = 9 \text{ kN}$, $n = 2000 \text{ min}^{-1}$ and $v_x = 10 \text{ mms}^{-1}$ AA 5083 displays a maximum shear stress of 77 MPa and AA 6082 of 54 MPa.

As for the shear strain, the stress values depend on the real thickness of the shear zone which is unknown at this point. Interestingly, higher strains correlate with lower shear stresses (Figure 7 (b)). The differences in the shear stresses calculated for the different parameter sets correlate well with the differences in average measured torque (compare Figure 5).

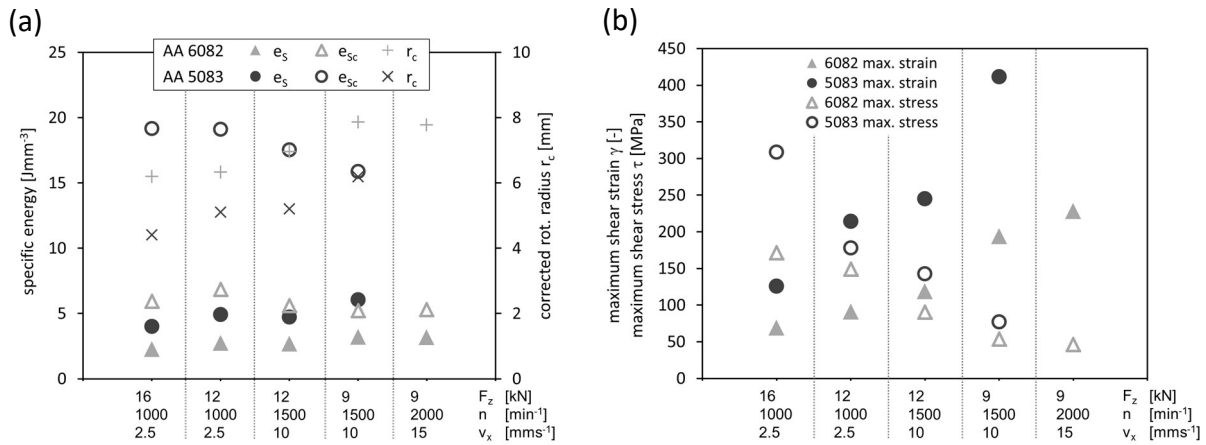


Figure 7: Corrected radius (r_c), nominal specific energy (e_s) and corrected specific energy (e_{sc}) introduced into the stud material during steady-state deposition (a); maximum shear strain and stress at the corrected radius r_c (b).

3.4 Process Temperatures

An image of the measurements obtained from the IR camera is presented in Figure 8 (a), showing the flash and the deposited coating. The temperature range displayed by the colour scale is 150 to 550°C; the stud is not visible since its temperature is below this range. The dashed line in the image marks the edge of the deposited layer, since a reflection of the hot stud and coating material on the substrate surface adjacent to the deposit is also recorded by the camera. The highest temperature in this thermogram (460°C) very clearly occurs in the shear zone between the rotating stud and the already deposited material underneath, which has cooled down to 310°C. The maximum temperature recorded during steady-state deposition, on the surface by IR camera and in the substrate-deposit interface by thermocouples, is shown in Figure 8 (b) for different process parameter sets. The maximum temperatures from the IR camera measurements, i.e. from the shear zone surface, are 15 to 35K higher for AA 6082 than for AA 5083 at the same parameters. For $F_z = 9$ kN, $n = 1500$ min⁻¹ and $v_x = 10$ mms⁻¹ both alloys show the highest maximum temperature.

The thermocouples in the interface between coating and substrate mostly display a lower temperature compared to the shear zone at each parameter set, due to fast heat conduction into the backing plate. A peculiarity are the very high temperatures measured in AA 5083 deposits at the low translational speed of $v_x = 2.5 \text{ mms}^{-1}$. Here, the process times are very long which leads to an accumulation of heat in the substrate, indicating a non-stationary state of the temperature field. For AA 6082, due to the fast stud consumption, the process at these parameter sets is very short and the generated heat does not lead to a pronounced increase in substrate temperature. It is intrinsic to the FS process that the temperature cannot be measured by standard methods exactly where it is generated, namely within the shear zone.

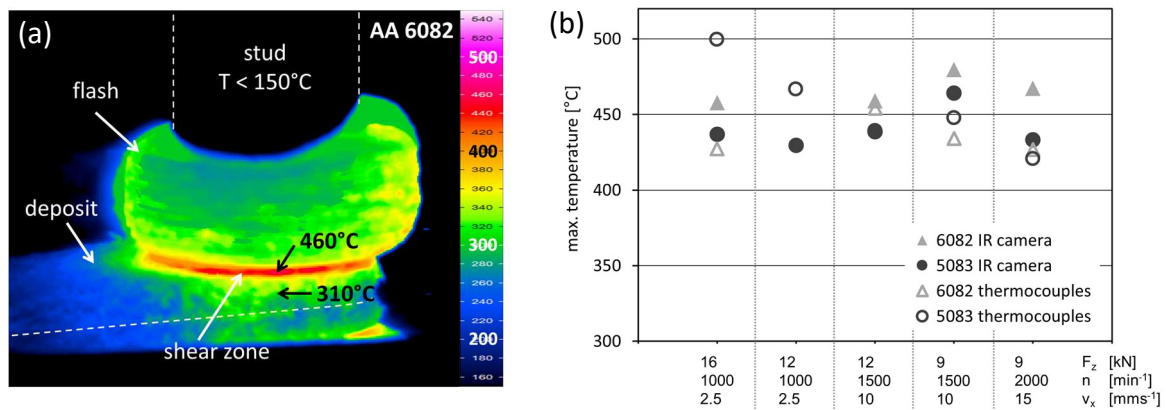


Figure 8: IR thermogram of ongoing process (AA 6082, $F_z = 9 \text{ kN}$, $n = 1500 \text{ min}^{-1}$, $v_x = 10 \text{ mms}^{-1}$); the coloured region below the dashed line is a reflection on the adjacent substrate surface (a). Maximum temperatures measured by thermocouples and IR camera during deposition (b).

3.5 Microstructure Analysis

The coatings' microstructure was examined by EBSD maps on cross sections perpendicular to the welding direction. Measurements were carried out in the cross section centre as well as at a distance of 6 mm from the centre towards the advancing side (AS) and retreating side (RS) as shown schematically in Figure 9. The AS is defined as the edge of the deposited layer at which the translational and rotational speed act in the same direction, while on the RS they are opposed to each other.



Figure 9: Polished cross section of AA 6082 layer deposited at $F_z = 9 \text{ kN}$, $n = 2000 \text{ min}^{-1}$ and $v_x = 15 \text{ mms}^{-1}$. Red squares indicate locations of EBSD maps in the centre and 6 mm each towards AS and RS.

Inverse pole figure (IPF) maps obtained from these locations are presented in Figure 10 to Figure 12. In these images high angle grain boundaries (HABs) of 15 to 65° misorientation are drawn as black lines, while bright pink lines indicate low angle boundaries (LABs) of 2 to 15° misorientation. Measurement points on precipitates were excluded and appear in black. The microstructure at the three different positions on a single deposit layer shows no obvious differences in grain size and morphology, except for locally varying preferred grain orientations (Figure 10 (a) and (b)). Equiaxed as well as grains elongated approximately in the main shear direction (parallel to the substrate surface) exist for both alloys, containing a high number of LABs. Grain fragmentation is observable; for AA 6082 with mainly straight, twin-like LABs separating the elongated grains across their shorter axis, and some equiaxed grains containing equally equiaxed subgrains. Due to the grain fragmentation, frequently neighbouring grains exhibit similar orientations (Figure 10). The substructure formed in AA 5083 seems to be finer with a more equiaxed morphology of both sub-grains and grains, but otherwise similar appearance (Figure 11). The grain sizes are also comparable for the two alloys, ranging between 2 and 5 μm and showing small variations between the deposited layers' surface and close to the substrate. Of the deposits generated at the same parameters shown in Figure 10 and Figure 11 (a) AA 6082 displays a slightly larger average grain diameter of $4.9 \pm 2.2 \mu\text{m}$ compared to AA 5083 with $3.3 \pm 1.8 \mu\text{m}$. For the AA 5083 deposit generated at lower translational speed shown in Figure 11 (b) the grain diameter exhibits an average value of $4.6 \pm 2.5 \mu\text{m}$.

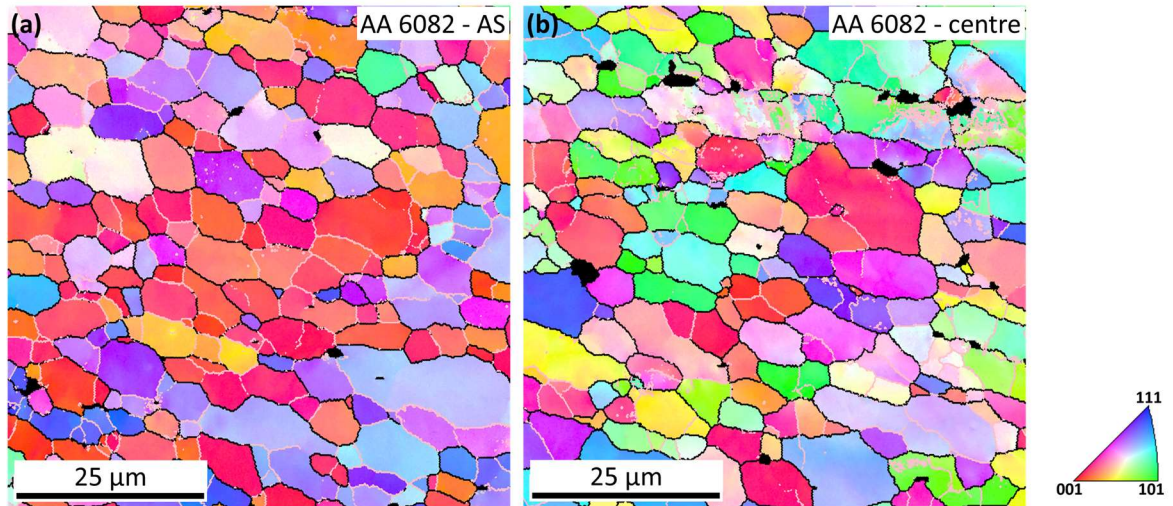


Figure 10: IPF maps from AS (a) and centre (b) on the cross section of an AA 6082 layer deposited at $F_z = 9 \text{ kN}$, $n = 1500 \text{ min}^{-1}$ and $v_x = 10 \text{ mms}^{-1}$.

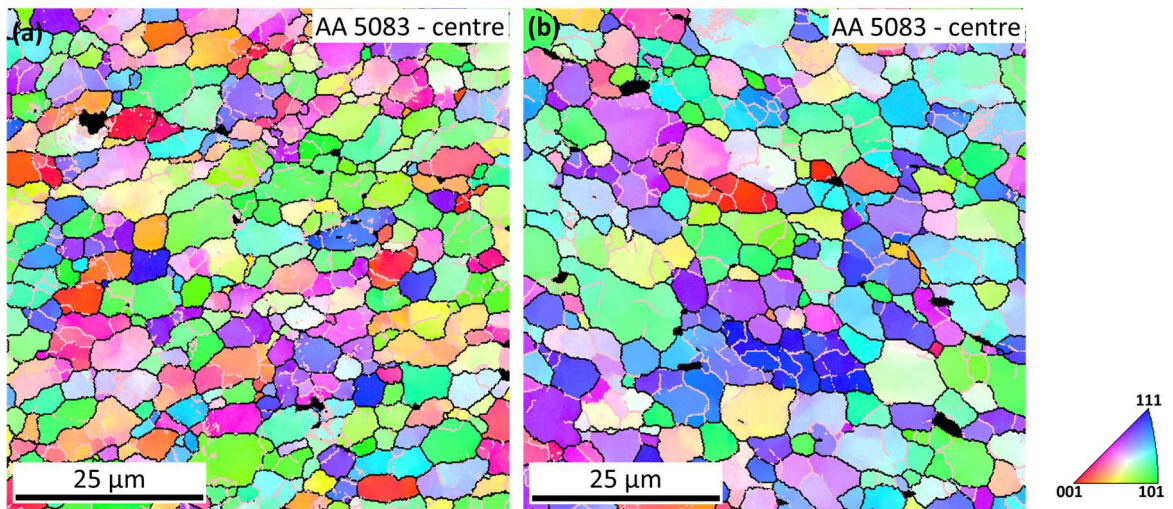


Figure 11: IPF maps from the centre of AA 5083 layers deposited at $F_z = 9 \text{ kN}$, $n = 1500 \text{ min}^{-1}$ and $v_x = 10 \text{ mms}^{-1}$ (a), and at $F_z = 16 \text{ kN}$, $n = 1000 \text{ min}^{-1}$ and $v_x = 2.5 \text{ mms}^{-1}$ (b).

In Figure 12 (a) the microstructure of AA 5083 deposited at low translational speed is shown at a higher magnification. In some locations the LABs in two neighbouring grains seem to be related (dashed circle). Such substructure forming across HABs may, under further deformation, transform into neighbouring grains sharing a common curvature of their HABs (solid circles). Further, signs of fragmentation of elongated grains along LABs by HAB migration of a neighbouring grain, as for example described by Renk et al. (2014), can be

observed and are marked by arrows. Dashed arrows point towards appearances of grain boundary bulging.

The grain size and boundary misorientation distributions in the centre of two deposits generated with the same parameter set are displayed in Figure 12 (b). For AA 5083 a peak in the graph of grain size distribution at $\approx 2.5 \mu\text{m}$ can be observed, while the distribution for AA 6082 is broader. The boundary misorientation of both alloys shows a high value at $\leq 3^\circ$, due to the residual strain and the LABs in the material. AA 5083 shows lower fractions of boundaries with small misorientation angles, which increase until $\approx 45^\circ$. While AA 6082 in general follows the same trend, again the distribution is clearly broader. These trends were also observed when comparing the two alloys processed at other parameters. At the parameter set shown in Figure 12 (b) AA 6082 exhibits 54% HABs $\geq 15^\circ$, while AA 5083 contains 60%. When comparing two deposits with similar layer geometry, 62% of boundaries display misorientations of $\geq 15^\circ$ for AA 5083 ($F_z = 16 \text{ kN}$, $n = 1000 \text{ min}^{-1}$, $v_x = 2.5 \text{ mms}^{-1}$), while AA 6082 ($F_z = 9 \text{ kN}$, $n = 2000 \text{ min}^{-1}$ and $v_x = 15 \text{ mms}^{-1}$) contains 63% HABs.

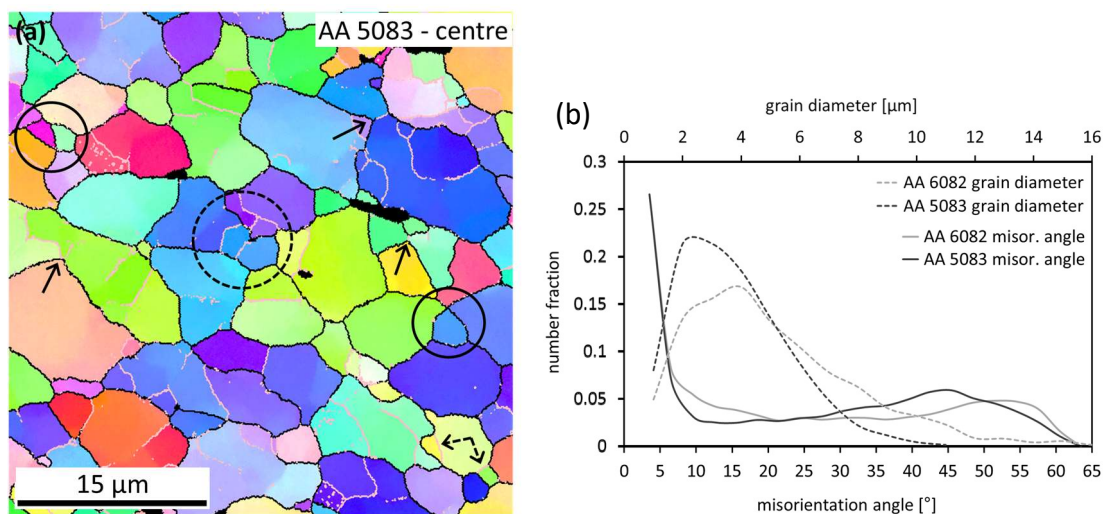


Figure 12: IPF map from the centre of AA 5083 deposited at $F_z = 16 \text{ kN}$, $n = 1000 \text{ min}^{-1}$ and $v_x = 2.5 \text{ mms}^{-1}$ (a). Boundary misorientation angles and grain diameter distribution in the centre of two deposits generated at $F_z = 9 \text{ kN}$, $n = 1500 \text{ min}^{-1}$ and $v_x = 10 \text{ mms}^{-1}$ (b).

4 Discussion

4.1 Specific Process Characteristics and Energy Input

From the direct comparison of the material behaviour and process characteristics of the two alloys during FS under the same conditions it becomes clear that AA 6082 delivers larger deposit volumes, less flash and can be processed at higher speeds. AA 6082 further always displays a higher torque, but a lower shear stress than AA 5083. The latter tends to develop process discontinuities or stud fracture due to force fluctuations at high process speeds, delivering only thin deposits. The trends in the development of e.g. deposit geometry or process torque with the parameters are the same for both alloys, varying only in the absolute values. The stud consumption rate is significantly higher and the nominal specific energy required to consume the stud material is significantly lower for AA 6082. It can therefore be clearly concluded that AA 6082 plasticises faster and with less energy required.

The specific energy required for FS may not be calculated precisely enough to correlate it with metallurgical mechanisms. Still, the calculated values ($\approx 60 \text{ kJmol}^{-1}$ for AA 6082 and $\approx 185 \text{ kJmol}^{-1}$ for AA 5083) are in the same order of magnitude as the activation energy for (thermal) self-diffusion, which lies at $\approx 120 \text{ kJmol}^{-1}$ for Al-Mg alloys with 1.1 to 3.3 at% Mg, as shown by Edalati et al. (2014) through comparing measured values gathered from literature. The activation energy is closely related to dislocation motion and correspondingly to dynamic recrystallization (DRX). Based on this observation, the differences in the required energy for FS may be related to changes in the DRX mechanisms or kinetics, caused by the different chemical composition of the two alloys.

4.2 Process Temperatures

The stud above the flash is not visible in the IR camera thermograms and therefore is at a temperature below 150°C . Assuming e.g. a stud consumption rate of $v_{\text{CR}} = 6 \text{ mms}^{-1}$, a flash height of 20 mm and a shear zone temperature of 450°C , the heating rate must be $> 90 \text{ Ks}^{-1}$. AA 5083 displays process temperatures 15 to 35 K lower than AA 6082, although there may be scatter involved in the measurements. The stud consumption rates of AA 5083 range at approximately 0.35 times those of AA 6082, thereby leaving significantly more time for the

stud material to reach a comparable process temperature. When processing AA 5083 by FS, clearly less heat is generated than when applying the same process parameters to AA 6082.

4.3 High-Temperature Material Strength

Available data for the high temperature, high strain rate mechanical properties of Al alloys are limited. The peak stresses presented in Table 2 imply that AA 5083 generally has the higher strength of the two alloys at elevated temperatures in tensile tests under a strain rate of 0.001 s^{-1} . For FS the flow stress is difficult to determine precisely, particularly because material flow into the flash in radial direction also occurs. Nevertheless, the approximated maximum torsional shear stresses, ≈ 75 to 310 MPa for AA 5083 and ≈ 50 to 160 MPa for AA 6082 (Figure 7 (b)), correspond roughly to the high-temperature properties reported in the literature for tensile tests (see Table 2: 30 and 75 MPa for AA 5083 and 14 to 42 MPa for AA 6082). The loading the material undergoes during FS is compression and torsional shear, and it can be assumed that the strain rates are higher than 0.001 s^{-1} . This explains the higher shear stresses observed in the present study. Material properties determined e.g. by high pressure torsion (HPT) would be more suitable in the discussion of the present findings, but the published data is very limited. Drury and Humphreys (1986) revealed in uniaxial compression tests on Al-5%Mg (similar to AA 5083) a stable constant flow stress of 60 MPa at 400°C and a strain rate of 0.002 s^{-1} for strains between 0.2 and 0.4 . This is again in a comparable range to the present findings but does not resemble the deformation conditions. In FS, similar to HPT, the applied pressure allows for the very high strains and the high temperature leads to DRX. The severe plastic deformation (SPD) during FS therefore takes place under steady-state DRX, implying that a constant flow stress – independent of the strain – should act. This flow stress is expected to depend on the strain rate and the process temperature only, which was described for various SPD processes in a review paper by Sakai et al. (2014). The maximum temperatures measured on the shear zone vary with different parameters, but in a rather narrow band (430 to 465°C for AA 5083 and 450 to 480°C for AA 6082). This is an indicator that a stable FS process depends on the existence of a specific material state, which seems to be achieved in a relatively narrow range of process temperatures. This specific state is reached by AA 6082 at lower shear strains under lower shear stress, than by AA 5083. The fact that the shear stress decreases with increasing

rotational speed and increasing strain (Figure 7 (b)) is contrary to the usual observations during SPD. If this is not behaviour specific for the extreme conditions encountered during FS, it could be explained by higher process temperatures within the shear zone than the ones measured from the outside. The uncertainty of not knowing the exact dimensions of the shear zone during processing may also play a role.

In order to acquire a shear zone located within the stud material it is necessary that the bonding strength of the softened stud tip material to the substrate surface is larger than the shear stress required for plastic torsional material flow. The necessity to reach a certain process temperature may therefore also be related to the corresponding low shear strain. This adhesion condition of the stud tip to the substrate is a characteristic of FS and does not apply e.g. to FSW in the same way.

4.4 Thermal Softening Behaviour

A discreet stud material volume, as it moves in z-direction towards the shear zone, is heated up from room temperature by thermal conduction at a heating rate which must be expected to increase as the shear zone is approached. Additionally, the material experiences the shear stresses. At a certain state of thermal softening the acting shear stress will be sufficient to induce torsional strain and finally intensive torsional material flow, which results in localized high heat generation constituting the shear zone. Therefore, not only the absolute high temperature flow stress of a material is relevant for the FS process but in particular its rate of thermal softening. The temperature dependent strength gradient along the stud axis is decisive for both the corrected radius as well as the shear localization, thereby influencing deposition efficiency and the dimensions of the shear zone. For Al-alloys the rate of thermal softening decreases with increasing content of Cu and Mg as observed in solidification experiments by Eskin et al. (2004). Since AA 5083 has a higher Mg content (4-4.9 wt%) than AA 6082 (0.6-1.2 wt%), it can be assumed that it exhibits a lower rate of thermal softening with increasing temperature. This may result in a continuous decrease of strength over a larger stud length, while AA 6082 may show a more rapid softening within a shorter section of the stud. As soon as the strength drops enough for the shear flow to set in heat will be generated in this location through viscous dissipation, resulting in further localization of the material flow. The growth or dissolution of strengthening precipitates in AA 6082 at increased

temperatures cause a further decrease in strength. Hence, AA 6082 would undergo more localized shear deformation and heat generation, while in the AA 5083 studs a large section undergoes low amounts of torsional strain before it forms or passes into a localized shear zone. The latter is less efficient with regard to the specific energy required to consume the stud. Another property known by experience to be relevant for FS is the thermal conductivity, which is higher for AA 6082 (see Table 2). While a higher thermal conductivity is typically assumed to counteract shear localization, it may on the other hand cause a steeper temperature gradient between the location of heat generation and the neighbouring material, which would further intensify differences in thermal softening rates.

4.5 Microstructure and Dynamic Recrystallization

Steady-state DRX during plastic deformation is commonly defined as a dynamic state of balance between strain hardening through dislocation generation and softening through recovery or recrystallization. This balance results in a constant flow stress with increasing strain for a given strain rate. The microstructure typically displays equiaxed, well defined subgrains of constant size and boundary misorientation with continuing deformation. At temperatures $> 0.5 T_{\text{melt}}$, this state is usually reached already after small strains < 1 , which was summarized by Zhilyaev et al. (2013) for various SPD processing methods.

During a stable FS process steady-state DRX takes place within the shear zone, resulting in constant torque and process reaction forces. Therefore, the microstructure in the deposits does not show distinct variations. Al-alloys possess high stacking fault energy and low shear modulus, which promotes dislocation movement and thereby recovery processes. At room temperature they generally undergo continuous DRX, also called dynamic recovery, which involves the formation of a cell structure which continuously transforms into high angle boundaries by the further intake of dislocations. The metallurgical processes involved in continuous DRX are described in detail by Sakai et al. (2014). A reduction of stacking fault energy, e.g. through a higher amount of dissolved foreign atoms, may result in a lower grain size due to a lower rate of dislocation annihilation. An increase in temperature will result in larger grains, since dislocations may annihilate faster and be less effective in the cell structure formation as shown in an investigation on the effects of adiabatic heating during SPD by Zhilyaev et al. (2013) and in a study on producing nanostructured aluminium alloys by Sabirov

et al. (2013). While these mechanisms are well understood for room temperature deformation at intermediate strains and strain rates, the mechanisms determining the microstructure formation at more extreme conditions are to date a matter of research. Current discussions of possible influences on dislocation and (sub)grain boundary movement include stress differences between neighbouring grains by Renk et al. (2014), solute atoms by Edalati et al. (2014) and segregations at grain boundaries by Sabirov et al. (2013).

The microstructure of the deposits shows typical appearances of continuous DRX, with fragmentation of larger grains through LABs, which transform to HABs of neighbouring grains with similar orientation. While many LABs in AA 6082 are straight, separating larger grains across their smaller axis, those in AA 5083 seem to be more equiaxed, which points to differences in the boundary energy and formation mechanisms. Sakai et al. (2014) argue that small grains at triple points, as visible in Figure 12 (a), may be part of other, larger grains in a different plane above or below the polished cross section, but could also stem from discontinuous recrystallization. Also, frequently winding HABs were found, which in other materials are considered typical appearances of grain boundary bulging and are also associated with discontinuous recrystallization mechanisms, e.g. by Li et al. (2011) in hot-deformed Inconel 625.

AA 6082 showed a broader distribution of boundary misorientations, with higher fractions of low angle boundaries than AA 5083 and a continuous increase of boundary misorientation with all angles existing at similar fractions. AA 5083 has a lower fraction of boundaries at misorientation angles $< 20^\circ$, and a high number at 45° . It appears that the transition from low to high misorientation occurs faster in AA 5083. Although the misorientation distribution shows differences between the alloys for all investigated samples, the overall fraction of LABs to HABs is mostly the same. Cleveland et al. (2003), who compared the superplastic behaviour of two aluminium alloys with different Mg contents, showed that a higher diffusivity caused by a higher Mg content (in this study of AA 5083) may enhance dislocation mobility. The higher content of solute atoms may on the other hand interfere with dislocation movement and in particular with their annihilation, as shown by the discussion of stacking fault energy changes through alloying elements by Edalati et al. (2014). AA 5083 must be processed slowly, in order to avoid process discontinuities, high lateral forces and risk of stud fracture. This

could be caused by a shift of the balance of dislocation generation and restoration mechanisms towards strain hardening for this alloy.

5 Conclusions

The following main conclusions can be drawn from this comparative study:

1. AA 6082 plasticises faster and with less energy required, leading to thicker and wider coatings and a higher material efficiency.
2. Process temperatures varied by 30K for each alloy within the parameter window of this study. Within this range a sufficient decrease in material strength is reached so that adhesion to the substrate is stronger than the shear stress within the shear zone. Process temperatures are 15 to 35K higher for AA 6082 and reached by lower strains than for AA 5083.
3. The specific energy required for FS is in the same order of magnitude as the activation energy for self-diffusion, which is closely related to DRX. DRX mechanisms or kinetics are affected by differences in chemical composition of the two alloys, and may contribute to the process behaviour.
4. The higher Mg content in AA 5083 leads to a lower rate of thermal softening with increasing temperature and a distribution of shear strain over a larger stud length. AA 6082 may undergo more localized shear, further intensified by a loss of strength through growth or dissolution of Mg_2Si with increasing temperature. This may contribute to a higher energy efficiency when plasticising AA 6082.
5. Microstructures of both alloys after FS are similar, with a tendency for lower average grain size and larger variations in grain boundary misorientations in AA 5083. A decrease in stacking fault energy and increase in diffusivity due to the higher content of Mg are possible influencing factors on DRX. The requirement of lower process speeds for AA 5083 points towards a shift in the steady-state DRX balance towards dislocation generation.

6 Acknowledgements

The authors wish to gratefully acknowledge the support and diligence of Tobias Bucken, University of Duisburg-Essen, in carrying out the FS experiments and collecting the data.

7 References

- Altenpohl, A., 2005. aluminium von innen, Aluminium-Verlag, Düsseldorf, pg. 427.
- Bedford, G.M., Vitanov, V.I., Voutchkov, I.I., 2001. On the thermo-mechanical events during friction surfacing of high speed steels. *Surface & Coatings Technology* 141, 34-39.
- Chandrasekaran, M., Batchelor, A.W., Jana, S., 1997. Study of the interfacial phenomena during friction surfacing of aluminium with steels. *Journal of Materials Science* 32, 6055-6062.
- Cleveland, R.M., Ghosh, A.K., Bradley, J.R., 2003. Comparison of superplastic behavior in two 5083 aluminum alloys. *Materials Science and Engineering A351*, 228-236.
- Darras, B.M., Abed, F.H., Abdul-Latif, A., Pervaiz, S., 2015. Experimental investigation of deformation in 5083 marine-grade aluminum alloy at elevated temperatures. *Journal of Materials Engineering and Performance* 24/4, 1663-1668.
- DIN EN 485-2:2013-12, Aluminium and aluminium alloys - Sheet, strip and plate - Part 2: Mechanical properties (2013).
- DIN EN 573-3:2013-12, Aluminium and aluminium alloys - Chemical composition and form of wrought products - Part 3: Chemical composition and form of products (2013).
- Donati, L., El Mehtedi, M., 2011. Characterization of flow stress of different AA6082 alloys by means of hot torsion test. In: *AIP Conference Proceedings* 1353, 455-460. DOI: 10.1063/1.3589557
- Drury, M.R., Humphreys, F.J., 1986. The development of microstructure in Al-5Mg during high temperature deformation. *Acta Metallurgica* 34/11, 2259-2271.
- Edalati, K., Akama, D., Nishio, A., Lee, S., Yonenaga, Y., Cubero-Sesin, J.M., Horita, Z., 2014. Influence of dislocation-solute atom interactions and stacking fault energy on grain size of single-phase alloys after severe plastic deformation using high-pressure torsion. *Acta Materialia* 69, 68-77.
- El-Danaf, E.A., AlMajid, A.A., Soliman, M.S., 2008. Hot deformation of AA6082-T4 aluminum alloy. *Journal of Materials Science* 43, 6324-6330.
- Eskin, D.G., Suyitno, Katgerman, L., 2004. Mechanical properties in the semi-solid state and hot tearing of aluminium alloys. *Progress in Materials Science* 49, 629-711.
- Fitseva, V., Krohn, H., Hanke, S., dos Santos, J.F., 2015. Friction surfacing of Ti-6Al-4V: Process characteristics and deposition behaviour at various rotational speeds. *Surface & Coatings Technology* 278, 56-63.
- Fitseva, V., Hanke, S., dos Santos, J.F., 2016. Influence of rotational speed on process characteristics, material flow and microstructure evolution in Friction Surfacing of Ti-6Al-4V. *Materials and Manufacturing Processes*, 2016, DOI:10.1080/10426914.2016.1257799.
- Fukakusa, K., 1996. On the characteristics of the rotational contact plane – A fundamental study of friction surfacing. *Welding International* 10/7, 524-529.
- Gandra, J., Pereira, D., Miranda, R.M., Vilaça, P., 2013. Influence of process parameters in the friction surfacing of AA 6082-T6 over AA 2024-T3. In: *Procedia CIRP* 7, 341 – 346
- Hanke, S., Fischer, A., Beyer, M., dos Santos, J., 2011. Cavitation erosion of NiAl-bronze layers generated by friction surfacing. *Wear* 273/1, 32-37
- Hanke, S., Beyer, M., Silvonen, A., dos Santos, J.F., Fischer, A., 2013. Cavitation erosion of Cr60Ni40 coatings generated by friction surfacing. *Wear* 301/1-2, 415-423.

- Hosseinipour, S.J., 2009. An investigation into hot deformability of aluminum alloy 5083. *Materials and Design* 30, 319-322.
- Li, D., Guo, Q., Guo, S., Peng, H., Wu, Z., 2011. The microstructure evolution and nucleation mechanisms of dynamic recrystallization in hot-deformed Inconel 625 superalloy. *Materials and Design* 32, 696-705.
- Liu, X.M., Zou, Z.D., Zhang, Y.H., Qu, S.Y., Wang, X.H., 2008. Transferring mechanism of the coating rod in friction surfacing. *Surface & Coatings Technology* 202, 1889-1894.
- Renk, O., Hohenwarter, A., Wurster, S., Pippan, R., 2014. Direct evidence for grain boundary motion as the dominant restoration mechanism in the steady-state regime of extremely cold-rolled copper. *Acta Materialia* 77, 401-410.
- Sabirov, I., Murashkin, M.Y., Valiev, R.Z., 2013. Nanostructured aluminium alloys produced by severe plastic deformation: New horizons in development. *Materials Science & Engineering A* 560, 1-24.
- Sakai, T., Belyakov, A., Kaibyshev, R., Miura, H., Jonas, J.J., 2014. Dynamic and post-dynamic recrystallization under hot, cold and severe plastic deformation. *Progress in Materials Science* 60, 130-207.
- Sakihama, H., Tokisue, H., Katoh, K., 2003. Mechanical properties of friction surfaced 5052 aluminum alloy. *Material Transactions* 44/12, 2688-2694.
- Shinoda, T., Li, J.Q., Katoh, Y., Yashiro, T., 1998. Effect of process parameters during friction coating on properties of non-dilution coating layers. *Surface Engineering* 14/3, 211-216.
- Soliman, M.S., El-Danaf, E.A., Almajid, A.A., 2010. Effect of heat treatment conditions on the high temperature deformation of 6082-Al alloy. *Advanced Materials Research* 83-86, 407-414.
- Suhuddin, U., Mironov, S., Krohn, H., Beyer, M., dos Santos, J.F., 2012. Microstructural evolution during friction surfacing of dissimilar aluminum alloys. *Metallurgical and Materials Transactions A* 43, 5224-5231.
- Tyayar, K.A., 1959. Friction welding in the reconditioning of worn components. *Svarochnoe Proizvodstov* 1/10, 71-76.
- Vitanov, V.I., Javaid, N., Stephenson, D.J., 2010. Application of response surface methodology for the optimisation of micro friction surfacing process. *Surface & Coatings Technology* 204, 3501-3508.
- Zhilyaev, A.P., Langdon, T.G., 2008. Using high-pressure torsion for metal processing: Fundamentals and applications. *Progress in Materials Science* 53, 893-979.
- Zhilyaev, A.P., Swaminathan, S., Pshenichnyuk, A.I., Langdon, T.G., McNelley, T.R., 2013. Adiabatic heating and the saturation of grain refinement during SPD of metals and alloys: experimental assessment and computer modelling. *Journal of Materials Science* 48, 4626-4636.